Revista de Metalurgia
January-March 2023, 59 (1), e236
ISSN-L: 0034-8570
https://doi.org/10.3989/revmetalm.236

Effect of yttria addition on the microstructure and mechanical behavior of ODS ferritic alloys processed by High Energy Milling and Spark Plasma Sintering

Ana R. Salazar-Román[a,*], Jorge López-Cuevas[a], Carlos R. Arganis-Juárez[b], José C. Méndez-García[c], Juan C. Rendón-Angeles[a], Sebastián Díaz-de la Torre[c]

[a] Centro de Investigación y de Estudios Avanzados del IPN (CINVESTAV), Unidad Saltillo. Industria Metalúrgica 1062, Parque Industrial, Ramos Arizpe 25900, Coahuila, México

[b] Instituto Nacional de Investigaciones Nucleares (ININ), Carretera México-Toluca s/n, La Marquesa Ocoyoacac, Estado de México 52750, México

[c] Instituto Politécnico Nacional, Centro de Investigación e Innovación Tecnológica (CIITEC). Cerrada Cecati s/n, Azcapotzalco, C.P. 02250 CDMX, México

(*Corresponding author: arsr2707@hotmail.com)

Submitted: 10 November 2022; Accepted: 11 March 2023; Available On-line: 27 April 2023

ABSTRACT: Oxide dispersion strengthened (ODS) ferritic alloys are structural materials used in nuclear fusion reactors, which exhibit enhanced mechanical properties, as well as corrosion and irradiation resistance. In the present work, ODS ferritic alloys with composition Fe-14Cr-1.5W-0.4Ti-(0, 0.4, 0.8) Y_2O_3 (in wt.%) were prepared employing high energy milling (HEM) followed by Spark Plasma Sintering (SPS). The particle size distribution (PSD) of the milled powders was characterized by laser diffraction. These powders and the sintered materials produced were characterized using X-ray diffraction (XRD), and scanning electron microscopy (SEM). The sintered materials were also characterized by dilatometry, diametral compression, Vickers microhardness, and corrosion rate tests. The largest Young's modulus, microhardness, and dimensional shrinkage/expansion were obtained for the 0.8 wt.% Y_2O_3 alloy. However, this alloy was the least ductile. Furthermore, the 0.8 wt.% Y_2O_3 alloy was the one with the least dimensional change. According to the potentiodynamic polarization studies, it was found that the protective layer of Cr_2O_3 formed on the surface of the three alloys studied was less effective for the yttria-free alloy, since in this case the rupture of such protective layer occurred earlier than for the case of the yttria-containing alloys. Based on these results, it is suggested that the 0.8 wt.% Y_2O_3 alloy having fine microstructure could constitute a potential alternative as a structural material for Gen IV-type reactors.

KEYWORDS: Corrosion; Powder; Sintering

Citation/Citar como: Salazar-Román, A.R.; López-Cuevas, J.; Arganis-Juárez, C.R.; Méndez-García, J.C.; Rendón-Angeles, J.C.; Díaz-de la Torre, S. (2023). "Effect of yttria addition on the microstructure and mechanical behavior of ODS ferritic alloys processed by High Energy Milling and Spark Plasma Sintering". *Rev. Metal.* 59(1): e236. https://doi.org/10.3989/revmetalm.236

RESUMEN. *Efecto de la adición de itria sobre la microestructura y comportamiento mecánico de aleaciones ferríticas ODS fabricadas por molienda de alta energía (HEM) y sinterización por arco eléctrico (SPS).* Las aleaciones ferríticas reforzadas con dispersión de óxido (ODS) son materiales estructurales utilizados en reactores de fusión nuclear, que exhiben propiedades mecánicas mejoradas, así como resistencia a la corrosión y a la irradiación. En el presente trabajo, se prepararon aleaciones ferríticas ODS con composición Fe-14Cr-1.5W-0.4Ti-(0; 0,4; 0,8) Y_2O_3 (en % en masa), empleando Molienda de Alta Energía (MAE) seguida de Sinterización por Plasma de Chispa (SPC). La distribución de tamaños de partículas (DTP) de los polvos mezclados y molidos se determinó utilizando difracción láser. Estos polvos y los materiales sinterizados se caracterizaron mediante difracción de rayos X (DRX), microscopía electrónica de barrido (MEB). Los materiales sinterizados también se caracterizaron utilizando dilatometría, compresión diametral, microdureza Vickers y test de corrosión. Los mayores valores del módulo de Young, microdureza y contracción/expansión dimensional fueron obtenidos para la aleación 0,8 wt.% Y_2O_3. Sin embargo, esta aleación fue la menos dúctil. Además, la aleación 0,8 wt.% Y_2O_3 fue la que presentó el menor cambio dimensional. De acuerdo con los estudios de polarización potenciodinámica realizados, se encontró que la capa protectora de Cr_2O_3 formada sobre la superficie de las tres aleaciones estudiadas fue menos efectiva para la aleación libre de itria, ya que en este caso la ruptura de dicha capa protectora se produjo antes que para el caso de las aleaciones que contienen itria. Con base en estos resultados, se sugiere que la aleación 0,8 wt.% Y_2O_3 con microestructura fina podría constituir una alternativa potencial como material estructural para reactores del tipo Gen IV.

PALABRAS CLAVE: Corrosión; Polvo; Sinterización

ORCID ID: Ana R. Salazar-Román (https://orcid.org/0000-0002-5663-4825); Jorge López-Cuevas (https://orcid.org/0000-0002-8287-0979); Carlos R. Arganis-Juárez (https://orcid.org/0000-0002-3846-7648); José C. Méndez-García (https://orcid.org/0000-0001-9211-1880); Juan C. Rendón-Angeles (https://orcid.org/0000-0003-4495-4503); Sebastián Díaz-de la Torre (https://orcid.org/0000-0003-0140-8342)

1. INTRODUCTION

The constant use of fossil fuels for energy production causes the emission of high volumes of CO_2 into the atmosphere (Perera, 2017). This has led to the search for CO_2-free alternative energy sources, such as nuclear. This, in turn, has generated the need to develop advanced materials that are safe to be used in the construction of nuclear reactors.

In the design and construction of nuclear reactors, some fundamental aspects should be considered. First of all, the performance of the materials is a key factor, since they will be subjected to conditions of high temperature and neutron irradiation (Zinkle and Busby, 2009); if they fail under such conditions, irreversible ecological-social-economical damages could be caused. In a socially responsible search for new structural materials, suitable for use in the fourth-generation nuclear reactors (Gen IV), oxide-dispersion-strengthened (ODS) ferritic steels are promising (Grimes *et al.*, 2008). In this sense, it is important to ensure the operating margin of the technological properties that will allow the ODS ferritic alloys to be used safely for this type of application, such as their corrosion behavior and mechanical resistance, both to swelling and to creep at high temperatures (Verhiest *et al.*, 2009).

In the current prototypes of nuclear fusion reactors, the ODS ferritic alloys are of great importance, since the dispersion of oxides within the alloy matrix contributes to the reduction of dislocations in its crystalline structure. Dispersed nano-oxides can occupy the sites of the defects in the material, which in turn eases the interaction of the latter with neutrons and helium ions, preventing its swelling and, therefore, preventing it from becoming brittle (Zinkle *et al.*, 2017). Powder metallurgy is a route often followed for the synthesis of these materials, as it ensures a homogeneous distribution of oxides in the alloy.

Within the extensive list of publications on ODS ferritic alloys that incorporate yttria dispersion, those mentioned in Table 1 have been designed for potential use in nuclear reactors. Table 1 includes representative publications that report the preparation of ODS ferritic alloys along with their synthesis conditions, as well as particle size and density achieved in the final products. The synthesis and consolidation techniques used for these powders include mechanical milling, sol-gel, spark plasma sintering, hot isostatic pressing, and hydrogen reduction. In some of these research works, a combination of processing techniques was employed. It is evident that depending on the synthesis and densification routes used, specific characteristics are conferred onto the resulting materials. From a general interpretation of the data reported in Table 1, it can be deduced that the dispersion of yttria particles in the matrix of the ferritic alloys increases their density, whereas their particle size is decreased.

The purpose of this work is to develop ferritic alloys of the type Fe-14Cr-1.5W-0.4Ti, with a dispersion of yttria particles in their matrix, in concentrations of 0, 0.4, and 0.8 wt.%, using a combination of high energy milling (HEM) and Spark Plasma Sintering (SPS), aiming to evaluate the effect of these oxide particles dispersion on the densification and physicochemical properties of the resulting alloys while preserving the fine grain size developed during the alloy processing.

Table 1. Publications reporting on the preparation of ODS ferritic alloys and their features

ODS Alloy (wt.%)	Processing technique and parameters[a]						Particle size (nm)	Relative Density (%)	Ref.
	Milling			Sintering					
	Atm	RPM	Time (h)	Heating rate (°C/ min)	Temp (°C)	Time (min)			
Fe-9Cr-1Mo (9CM) Fe-9Cr-1Mo-0.5Y_2O_3 (9CMY)	PBM	-	20	SPS	600, to 800	2 to 60	9 CM 14-18 9 CMY 15000-34000	9 CM 9 CMY 63 - 64 76 - 79 87 - 89	(Rajan *et al.*, 2013)
Fe-14Cr-0.4Ti+0.25 Y_2O_3	Ar PBM	150	60	SPS (100)	1150	18.5	500 1000-2000	99.6	
(All with 1 wt.% Y_2O_3) (A) Fe–13.5Cr–2Al–0.5Ti (B) Fe–17.5Cr–2Al–0.5Ti (C) Fe–21.5Cr–2Al–0.5Ti (D) Fe–25.5Cr–2Al–0.5Ti	PBM	300	40	SPS	600, to 1000	5	$Y_2Ti_2O_7$ 10-20	1000 °C (A) 99.8 (B) 99.7 (C) 99.7 (D) 99.5	(Karak *et al.*, 2012)
(All with Fe-9Cr-) 1Mo (9CM) 1Mo– 0.5Y_2O_3 (9CMY) 1Mo–0.25Ti–0.5Y_2O_3 (9CMYT) 1W (9CW) 1W–0.5Y_2O_3 (9CWY) 1W–0.5Y_2O_3–0.25Ti (9CWYT)	PBM	300	20	SPS (100)	700	9.7	Grain size 383 (9CM) 360 (9 CMY) 310 (9 CMYT) 390 (9 CW) 378 (9 CWY) 326 (9 CWYT)	>99	(Rajan *et al.*, 2012)
84Fe–14Cr–2Y_2O_3	Ar PBM	1100	0.16-1.5	SPS	1100	30	1000-32000 1000-25000	-	(Park *et al.*, 2012)
Fe-14Cr-0.4Ti-0.25Y_2O_3	Ar PBM	300 and 350	23	SPS (150)	450 (PC) 1100	5	Crystallite 10	99.3	(Mihalache *et al.*, 2019)
Fe-18Cr-2W-0.25Ti-0.1C-0.35Y_2O_3	Ar PBM	300	6	SPS	1000-1150	15	10000	96.7 98.7	(Dash *et al.*, 2018)
Fe-14Cr-3W-0.2Ti-0.3Y	sol-gel H_{RED}	110 550 1200 °C	12 5 3	SPS (100)	1100	5	$Y_2Ti_7O_7$ Crystallite 55	97	(Sun *et al.*, 2012)

ODS Alloy (wt.%)	Processing technique and parameters[a]						Particle size (nm)	Relative Density (%)	Ref.
	Milling			Sintering					
	Atm	RPM	Time (h)	Heating rate (°C/ min)	Temp (°C)	Time (min)			
Fe-14Cr-2W-0.4Ti-0.25Y_2O_3	GAP Ar PBM	150 and 250	20	SPS	1050	3	1.5-25	-	(Auger *et al.*, 2013)
Fe-16Cr-2W-0.5Ti-0.4Y_2O_3-4Al-1.0Zr	H sol-gel Ar PBM	120 300 1050 680 °C 3 rpm	10 3.5 10 3 20	SPS (100)	1200	8	25	98.6	(Gao *et al.*, 2014)
Fe–14Cr–2W–0.3Ti–0.3Y_2O_3	Ar GAP H PBM	-	48	HE HR HT	1100 700 1050	1	Y–Ti–O 5	-	(Oksiuta *et al.*, 2009)
Fe-18Cr-2 W0.2Ti Fe-18Cr-2 W-0.2Ti-0.35Y_2O_3	Ar HEM	1000	7 120 cyclic	H PLS (15)	1200	3.13	550-700	99.86	(Kumar *et al.*, 2017)
Fe–16.5Cr–0.89Mn-0.3Y_2O_3 -2ZrO_2 Fe–16.5Cr–0.89Mn-0.3Y_2O_3 -2ZrO_2 -2Al	Air PBM	300	20	HP (5)	1170	5.4	Crystallite size 2.6-3.5	96	(Dharma-lingam, *et al.*, 2018)
Fe-15Cr-1Mo-0.3Ti-0.35Y_2O_3	Ar, H, HEM	240	48	HIP (5) HR	1150 1150	3 1	40000 to 100000	-	(Noh *et al.*, 2014)
Fe-14Cr-1W-0.4Ti-0.3Mn-0.3Si-0.15Ni (0, 0.3, 0.6 Y_2O_3)	Ar PBM HEM	250 800-1200	20 24, 48 and 80	SPS HE HIP	1050 1150	0.16 1	1.5	99	(Hilger *et al.*, 2016)
Fe-20Cr-5Al+-Ti- Y_2O_3 Fe-14Cr-5Al-3W+Ti-Y_2O_3	Ar HEM	900	30	SPS (100)	1200	13	Crystallite size 14.1 and 11.4	91.3 91.8	(Torralba *et al.*, 2013)
Fe-9Cr-1.1W0.4Mn-0.2V-0.12Ta-0.3Y_2O_3	Ar PBM	300	6 and 36	SPS (50-400)	1050 1100 1150	3.38	10000-50000	99	(Fu *et al.*, 2019)
Fe-14Cr-1.5W-0.2Ti-(0, 0.4, 0.8 Y_2O_3)	Air	900	1	SPS (200)	1100	5.5	330 1340 2760	94.5	This work[a]

[a]PBM: Planetary ball mill; HEM: High-energy milling; HEA: High-energy attrition; GAP: Gas Atomization Pressure; SPS: Spark plasma sintering; HIP: Hot isostatic pressing, and H_{RED}: Hydrogen reduction.

2. MATERIALS AND METHODS

2.1. High energy milling

For this investigation, the following reagent-grade commercial powders were acquired from Sigma Aldrich company (particle size and purity, in wt.%, are indicated inside the parentheses): Fe (83 μm, 99%), Cr (45 μm, 99%), W (12 μm, 99.9%), Ti (5-10 μm, 99.9%), Y_2O_3 (5.3 μm, 99.9%), and $C_{18}H_{36}O_2$. The latter material (stearic acid) was used as a lubricant or process control agent (PCA) during milling, setting 0.2 g per batch. To analyze the effect of the amount of added yttria on both the sintering process and the resulting properties of the ODS ferritic alloys, three compositions were prepared (see Table 2).

Table 2. Admixture codes and chemical composition of the synthesized ODS ferritic alloys (wt.%)

Mixture code	Fe	Cr	W	Ti	Y_2O_3
0 wt.% Y_2O_3	Bal	14	1.5	0.4	0
0.4 wt.% Y_2O_3	Bal	14	1.5	0.4	0.4
0.8 wt.% Y_2O_3	Bal	14	1.5	0.4	0.8

Selected compositions were thoroughly milled using a commercial HEM mill (Simoloyer, Zoz GmbH CM01), operated in an air atmosphere with yttria-stabilized zirconia balls of 10 mm in diameter, and with a balls/powder weight ratio of 40:1. The milling cycles were carried out for 15, 30, 45 and 60 min at 900 rpm.

2.2. Spark Plasma Sintering

As for the sintering runs, a commercial SPS device (Sumitomoto Dr. Sinter, SPS-1050) was used, operating at high vacuum conditions under on/off current pulses of 12/2, as well as 3500 Amp, 4 V, 60 Hz, and 6 kN axial load. Using the latter technique, 4.5 g of each of the milled powder series was densified, using graphite cylindrical dies with an inner and external diameter of 10 and 50 mm, respectively. The sintering runs were conducted at a heating rate of 200 $^oC \cdot min^{-1}$ up to 1100 ^oC, with no holding time at the peak temperature, obtaining sintered coin-like specimens 10 mm in diameter and 7 mm high. The total sintering time was 5.5 min per sample.

2.3. Characterization of milled powders

To study the effect of milling time on the particle size, a particle size distribution (PSD) analysis was performed using a Horiba apparatus, model LA950V2, employing ethanol as dispersing medium. To monitor any changes in the crystalline structure of the powders, X-ray diffraction analysis (XRD, Bruker model D8 Advance Echo, CuKα radiation, λ = 1.5406 Å, 2θ = 20-100°, 0.6 mm slit, and step size of 0.02° with a duration of 0.3 s per step) was carried out. The crystallite size and lattice parameter of the α-Fe phase were determined for the 0 ODS powder as well as for the sintered alloys containing 0, 0.4, and 0.8 wt.% Y_2O_3 from the corresponding XRD patterns by Rietveld refinement, using the Panalytical's HighScore Plus software, and the size-strain analysis routine. Details of the crystal structure of the phases were obtained from the COD and ICDD databases.

2.4. Characterization of Sintered Samples

A SEM (JEOL JSM-7600-F, field emission) microscope was used to analyze the morphological evolution of the milled powder, as well as the microstructure of the sintered samples. The sintered specimens were prepared for SEM analysis following standard metallographic techniques. The relative density of the sintered specimens was measured by the Archimedes' principle in distilled water. Their Vickers microhardness was determined using a Shimadzu HMV-G 20DT apparatus, under a load of 100 g for 10 sec ($HV_{0.1}$). To determine the phase transformations occurring in the studied materials, samples of 9x4x3 mm were prepared by cutting the sintered specimens with diamond discs, and then analyzing using a quenching dilatometer (Linseis Model L78 Rapid Induction Thermal Analysis). The analysis conditions consisted of heating and cooling rates of 10 $°C \cdot s^{-1}$, a temperature range of 25-1100 °C, no holding time at the peak temperature, helium atmosphere, and chromel-alumel thermocouples for temperature measurements.

Corrosion tests were carried out using a 1 M HNO_3 solution, a 3.8 M Ag/AgCl reference electrode (199 mV vs. Standard Hydrogen Electrode, SHE), and a graphite bar as the counter electrode. The failure analysis of the material due to its susceptibility to corrosion was carried out using the "Tafel technique and polarization curves" (Buchanan and Stansbury, 2012). The reason for using HNO_3 to conduct the corrosion tests of the studied alloys is that it is an aggressive oxidant that is typically used in the separation of spent fuel from nuclear fission reactors in the "Purex process" (Ramanujam, 2001). Before the electrochemical analysis, the alloys were mounted in epoxy resin, which was perforated to ensure good electrical contact between the sample, electrolyte, and working electrode. The test area of the samples was 0.785 cm^2. In conducting the corrosion tests, a commercial ACM Instruments model Gill AC equipment was used, following the electrochemical polarization technique (Buchanan and Stansbury, 2012), establishing an electrochemical sweep range of -250 to 250 mV versus the resting potential, at a rate of 10 $mV \cdot min^{-1}$.

To determine the Young's and Poisson's elastic moduli of the alloys under study, the diametral compression test was employed, for which two strain gaug-

es with 2.11 NOM gauge factor were used, that were placed longitudinally and transversely on each one of the specimens tested. The compression tests were conducted using a Universal 647 Hydraulic Wedge Grip machine, MTS Landmark, coupled to a p3 Strain Indicator - Record equipment, to obtain the values of transverse and longitudinal micro deformations, for each compression tested material.

3. RESULTS AND DISCUSSION

3.1. Characterization of Milled Powders

From the PSD analysis, reported in Fig. 1a – 1c, it can be confirmed that in general, the particle size distribution of the alloy series prepared in this work is both multi-sized and multi-modal at the beginning of the milling stage, whereas it tends to be monomodal towards the end of the milling time. The mean particle size of all initial admixtures of elemental powders, i.e., without milling, is smaller than that obtained after 15 to 30 min of mechanical alloying, the lapse in which particle agglomeration predominantly occurs. After around 15 min of the high-energy milling process of the studied system, no apparent effect of yttria content on the alloying mechanism that occurs between chemical elements interacting in the solid state is observed, at least not in the particle size distribution reached (agglomerates of 175 microns). Regardless of the amount of yttria present in the powdered ferritic alloy, no difference is observed between the PSD curves (red) of these three cases (Figs. 1a- 1c). The first clear evidence of the PSD change is observed after 30 min of milling (blue lines) when the yttria content is 0.4 wt.%, revealed by a slight left-shift of the curves towards a smaller particle size (Fig. 1a). In addition, after milling for 45 min under the established conditions, the 0.4 wt.% yttria particles appear to have a preferential influence, narrowing the monomodal geometry of the particles and decreasing their size to approximately 25 µm. In general, from Fig. 1 we can conclude that, even if yttria particles have been added to the ferritic alloy or not, the final size of the particles is less than 20 µm, after 60 min milling. However, it should be noted that even when the three series of alloys were successfully refined and homogenized, the yttria content between them is different and the 0.4 wt% series revealed the highest percentage cumulative volume of particles.

It is remarkable that the absence of yttria in the powdered alloy obtained after the mechanical alloying is associated with a mean particle size up to 35% smaller than that obtained with the addition of yttria. Compared with other investigations in which HEM was not used, but rather conventional milling in a planetary ball mill (Hilger *et al.*, 2015), in our work, a 60% smaller particle size, was achieved, in a considerably shorter milling time. Figure 2 shows

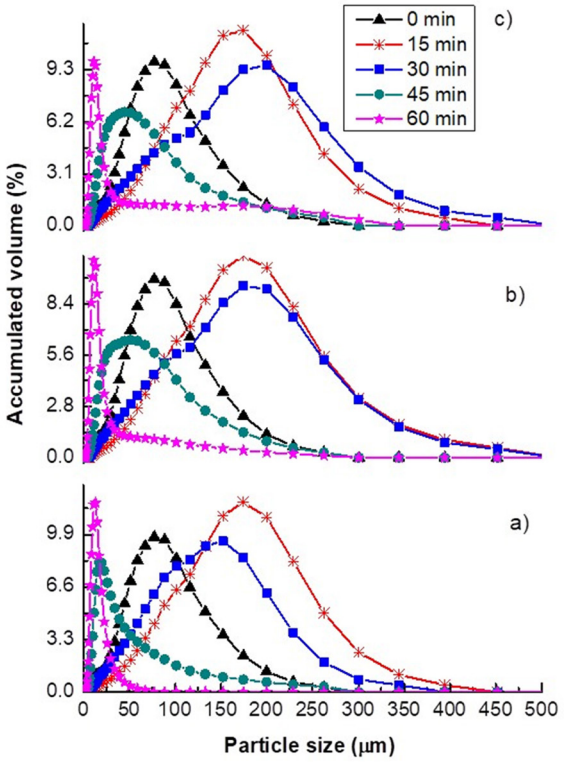

Figure 1. Variation of particle size vs accumulated volume, as a function of milling time, for the ODS ferritic alloy containing: a) 0.4, b) 0.8, and c) 0 wt.% Y_2O_3.

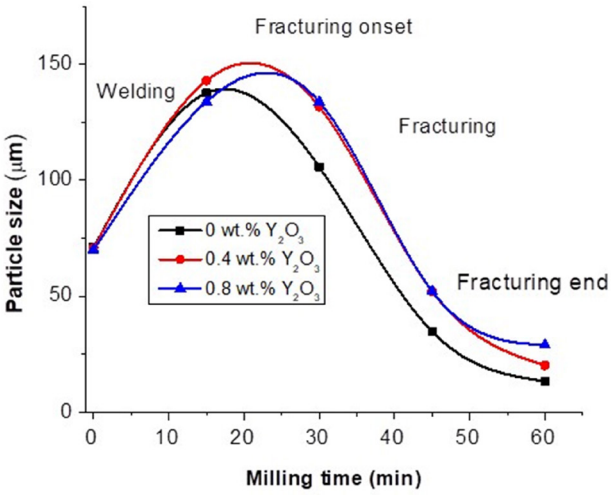

Figure 2. Evolution of the particle size for the three studied series of ODS ferritic alloys containing the percentage of yttria indicated plotted as a function of milling time. Yttria addition seems to hinder particle refinement.

the mean particle size evolution obtained from the PDS analysis. Previously, from the experimental data used to plot Fig. 1, it was noticed that, even though PSD curves with bimodal behavior were recorded even after milling for 60 min, both a more

homogeneous distribution and the finest particle size were achieved. A separation of the overlapped PSD curves was carried out using the Fityk data analysis program, for the three alloys milled for 60 min. It was found that the powder of the yttria-free alloy contains particles whose sizes ranged from 8 to 33 µm, whereas those for the alloy with 0.4 wt.% Y_2O_3 ranged from 20 to 134 µm, and those for the alloy with 0.8 wt.% Y_2O_3 ranged from 40 to 276 µm. From these results, it can be observed that the addition of yttria to the studied alloy entails a substantial increase in its particle size, making it difficult to be refined.

Figures 3 to 5 show respectively the XRD patterns of the powdered alloys containing 0.4, 0.8 and 0 wt.% Y_2O_3. All these figures show the same trend, as the mechanical milling time advances, the broadening of the peaks (FWHM, full width at half-maximum intensity) increases, which indicates a decrease in the crystallite size of the ferritic matrix (Dash *et al.*, 2018). In these XRD patterns, overlapping of the diffraction peaks occurred due to the presence of chromium traces and α-Fe in the alloy's matrix, whose diffraction angles are very close to each other. The presence of yttria is not observed in the XRD patterns of Figs. 3 and 5, since it was added in such a proportion that it was below the detection limit of this technique (Sun *et al.*, 2012).

As for the lattice parameter and crystallite size of the α-Fe phase present in the ODS alloys, as can be seen in Fig. 6, in the case of the powdered alloy

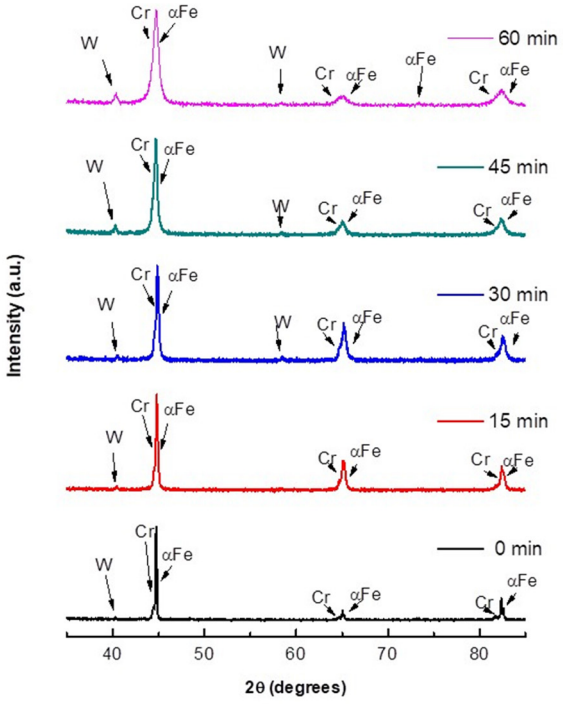

Figure 3. XRD patterns of powders of the 0.4 wt.% Y_2O_3 alloy processed by HEM for the indicated times.

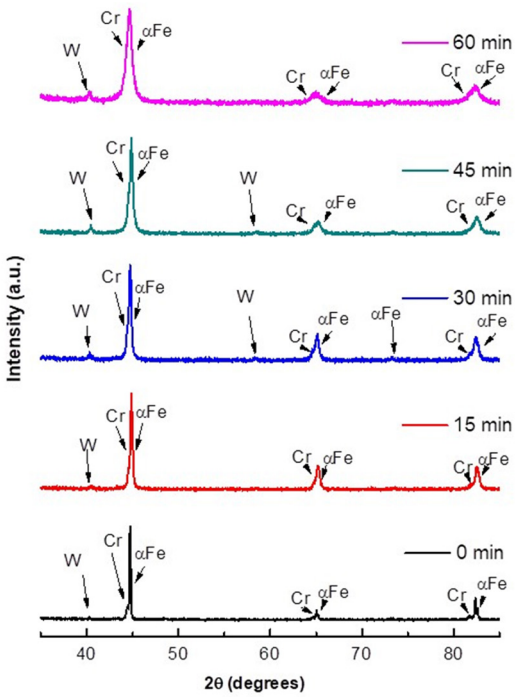

Figure 4. XRD patterns of powders of the 0.8 wt.% Y_2O_3 alloy processed by HEM for the indicated times.

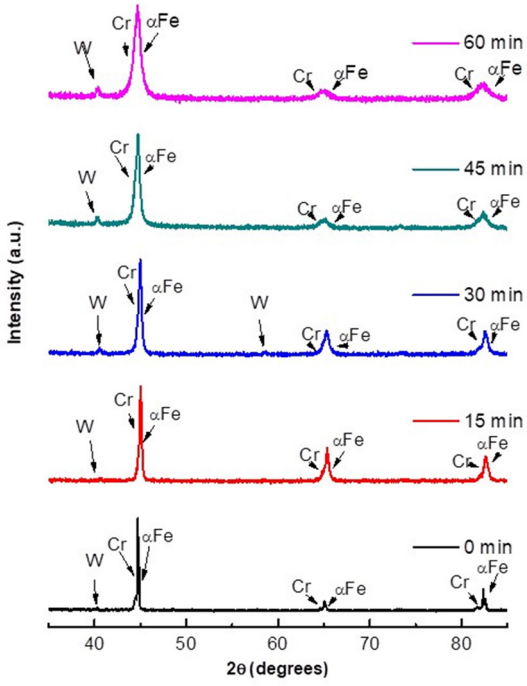

Figure 5. XRD patterns of powders of the Y_2O_3-free alloy processed by HEM for the indicated times.

without Y_2O_3 and no sintering (0 NS), the lattice parameter and crystallite size of the α-Fe phase was 0.286 nm and 500 nm, respectively. After sintering,

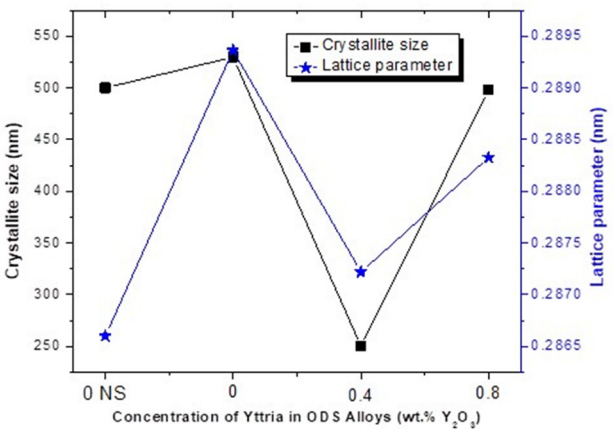

Figure 6. Evolution of the lattice parameter and crystallite size of the α-Fe phase as a function of Y_2O_3concentration (wt.%) for the Y_2O_3-free alloy without sintering (0 NS), as well as for the sintered Y_2O_3-free, 0.4 wt.% Y_2O_3 and 0.8 wt.% Y_2O_3 alloys.

this alloy showed an increase in the lattice parameter to 0.289 nm, indicating dissolution of the alloying elements into its ferritic matrix with sintering.

Now, for the alloy containing 0.4 wt.% Y_2O_3, both the lattice parameter and the crystallite size decreased to 0.2872 and 250 nm, respectively, indicating a refinement of the grain size of the ferritic matrix of the alloy (Cayron *et al.*, 2004). For the alloy containing 0.8 wt.% Y_2O_3, there was an increment in both the lattice parameter and crystallite size to 0.288 and 498 nm, respectively. The abrupt change in the magnitudes of those parameters requires further investigation.

Figure 7 shows a sequence of SEM micrographs taken from the studied powder as a function of the milling time. The morphology changes followed by the admixture of precursor powders are evident. As it was mentioned in the previous section on the PSD analysis, between 15 and 30 min of milling, the particle´s growth is clear, which is nothing but the agglomeration of the particles. As for the alloy having no yttria (series 1), it can be observed that after 30 min of milling the particles, they become flakier, unlike the two yttria-containing alloys (series 2 and 3). From this observation, it can be suggested that, for the case of the yttria-containing alloys, after 45 min of milling the materials experienced cold deformation hardening, eventually fragmenting into smaller particles. For the alloy lacking yttria (series 1), it can be noted that the particles processed at 45 (c1) and 60 min (d1) are similar in shape and size to each other, which indicates that the fracture process between particles tends to stabilize after 45 min. Other authors (Fu *et al.*, 2019), who did not use high-energy milling, reported that the stable process

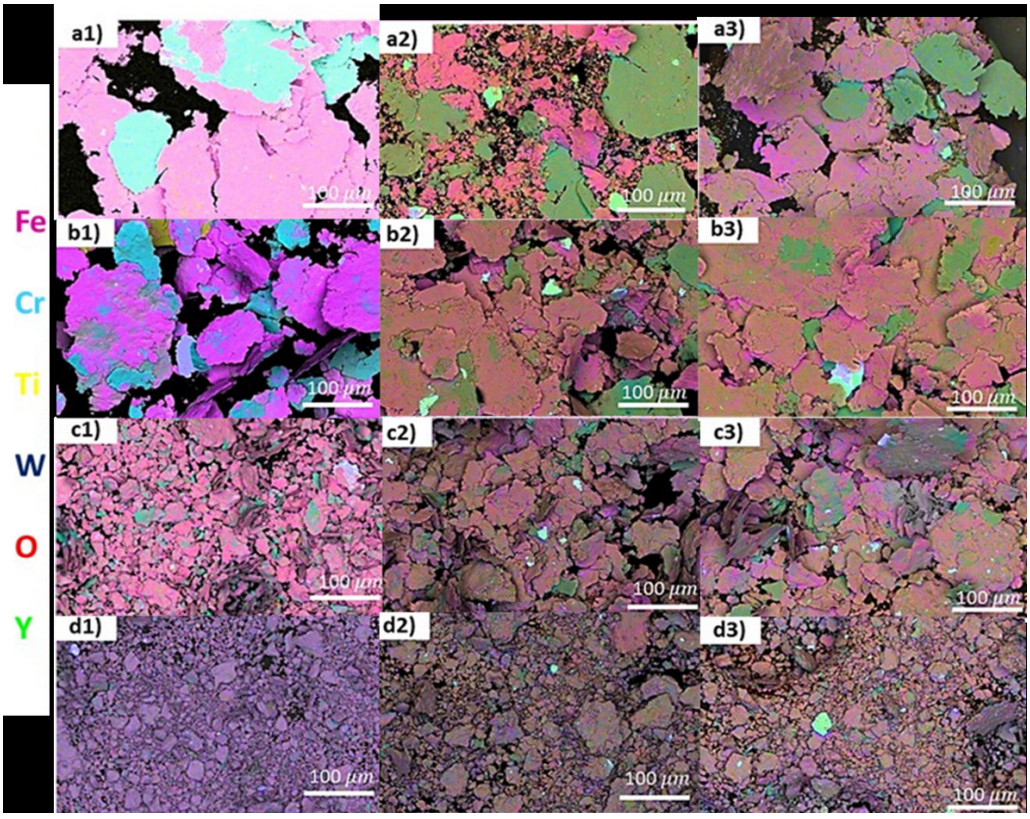

Figure 7. SEM micrographs of powders processed by HEM, corresponding to the ODS alloy series containing: 1) 0, 2) 0.4, and 3) 0.8 wt.% Y_2O_3, with milling times of: a) 15, b) 30, c) 45 and d) 60 min.

for a ferritic alloy with oxide dispersion is reached after 13 h, meanwhile, in this work using HEM, such stability is achieved in 45 min, which significantly reduces energy and thus cost.

3.2. Characterization of sintered alloys

The phase changes undergone by the ODS alloys heated up to 1100 °C were recorded by dilatometry. In Fig. 8, the T_1, T_3, and T_5 points show the temperature at which the phase transformation from ferrite to austenite ($\alpha \rightarrow \gamma$) begins. Points T_2, T_4, and T_6 correspond to the final temperature of such transformation (Cayron *et al.*, 2004), for the ODS ferritic alloys with 0.4, 0.8, and 0 wt.% Y_2O_3, respectively. Points T_{M1}, T_{M2}, and T_{M3} correspond to the temperature at which the martensitic transformation occurs for the three alloys, respectively. Figure 8 allows verifying that the ODS ferritic alloys with 0 and 0.8 wt.% Y_2O_3 have similar behavior to each other, regarding their linear thermal expansion (dL/L_o). However, the initial $\alpha \rightarrow \gamma$ transformation temperature is lower for the alloy without yttria (T_5 = 760 °C). Comparatively, in the case of the alloy with 0.4 wt.% Y_2O_3, such a phase transition begins at 820 °C ($T_1 = T_3$), extending up to 860 °C (T_2), which is associated with a linear thermal expansion ΔL approximately 12.5% higher than that for its counterparts with 0 and 0.8 wt.% Y_2O_3. In the case of these last two alloys, the ferrite structure is more stable and therefore it does not fully transform into austenite.

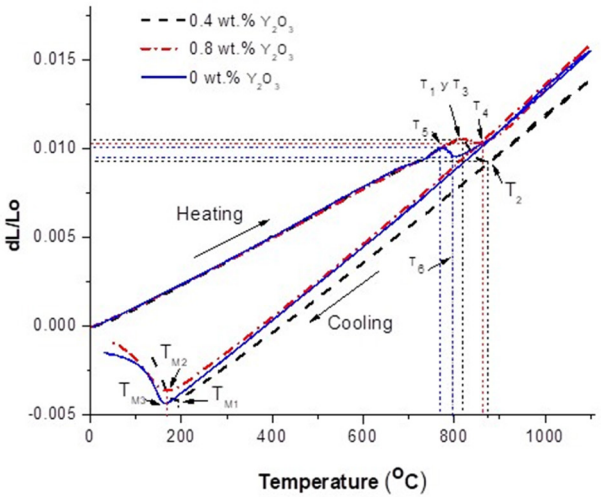

Figure 8. Thermal dilatometry curves as obtained for the ODS ferritic alloys containing 0, 0.4 and 0.8 wt.% Y_2O_3. T1, T3 and T5 show the onset transition temperature from ferrite to austenite ($\alpha \rightarrow \gamma$). Points T2, T4 and T6 matches the end of such transition. TM1, TM2 and TM3 indicate the martensitic transformation for the three alloys, respectively. In the case of 0 and 0.8 wt,% Y_2O_3 alloys, the ferrite structure is more stable, whereby it does not fully transform into austenite.

Yamamoto *et al.* (2010) added 0.35 and 0.7 wt.% Y_2O_3 to an alloy Fe-0.13C-2W-0.2Ti, finding by mathematical simulation that the speed of movement of the ferrite-austenite interface decreases by the dragging of oxide particles. On the other hand, Kumar *et al.* (2018) concluded that contents of Y_2O_3 higher than 0.5 wt.% lead to the production of materials with high hardness and high elastic modulus due to work hardening, generating microcracks that cause fractures, and, therefore, a lower ductility in the material. The probable occurrence of all these phenomena in our series of ferritic alloys analyzed is high, particularly in the one with the highest percentage (0.8 wt.%) of Y_2O_3. This is explained by the fact that this oxide acts as an element that not only anchors microstructural defects, with the consequent hardening of the alloy but also prevents the linear thermal expansion of the material. Considering that yttria is a ceramic with predominantly ionic-covalent and non-metallic bonds, it is expected that its presence in the metallic matrix reduces the longitudinal elongation of the entire specimen.

Regarding the martensitic phase transformation (γ - α') (Zhou *et al.*, 2017), it first took place in the 0.4 wt.% Y_2O_3 alloy during the cooling stage (T_{M1} = 188 °C), while in the 0 and 0.8 wt.% Y_2O_3 alloys (blue and red curves in Fig. 8, respectively) it happened at the same lower temperature ($T_{M2} = T_{M3}$ = 165 °C). Since the latter two alloys have a similar dilatometric behavior they disclosed a 10% difference concerning their starting temperature, for the $\alpha \rightarrow \gamma$ transformation. Since, according to Fig. 8, the largest area under the heating and cooling curves corresponds to the ODS alloy with 0.4 wt.% Y_2O_3, it follows that this material is the one undergoing the greatest thermal expansion among all the alloys studied.

In general, it was expected to find a marked influence between the yttria content and the formation of martensite, and therefore on its mechanical properties. In practice, however, the obtained alloys showed a positive effect of yttria regarding their performance against corrosion and adequate mechanical resistance.

In this way, the temperature that indicates the start of the martensitic transformation (T_M) is practically the same for two of the alloys studied ($T_{M2} = T_{M3}$), presenting only a negligible difference of 23 °C concerning the alloy with 0.4 wt.% of Y_2O_3, being greater for the latter alloy. The value of T_M is rather related to the grain size of the austenite, as well as the amount of available ferrite (Zhou *et al.*, 2017). As it has been mentioned, the alloy with 0.4 wt.% Y_2O_3 presents the highest amount of austenite, therefore, it exhibits the highest dimensional change during cooling.

On average, the relative density (RD) attained by the alloys prepared in this work is above 93%, which is higher than the results reported by other authors

(Mihalache *et al.*, 2019), who also used SPS sintering (for a Fe-14Cr-0.4Ti-0.25Y_2O_3 alloy). The RD values obtained for the 0, 0.4, and 0.8 wt.% Y_2O_3 alloys of this study are 7.8, 7.5, and 8.5%, respectively. Fu *et al.* (2019) reported lower RD values (5.2, 5.5, and 4.5%) for a Fe-9Cr-1.1W-0.4Mn-0.2V-0.12Ta-0.3Y_2O_3 alloy. Other research works (Abenojar *et al.*, 2006), in which the 90Fe/10B_4C alloy was sintered using conventional techniques, without oxide dispersion, and also considering potential applications in nuclear reactors, report RD values which are 13.0, 12.6, and 13.8% lower than those here reported. The density values obtained for the alloys in this work are similar to those reported by other authors (for a Fe-14Cr-0.4Ti-0.25Y_2O_3 alloy) (Zhang *et al.*, 2015), who also used SPS and who, unlike the present study, did consider a holding time at the peak sintering temperature.

In the practice of this work, both the morphology and the particle size distribution directly affect the degree of densification achievable during the sintering process. The addition of 0.8 wt.% Y_2O_3 to the ferritic alloy leads to an increase in its relative density (up to a value of 94.5%), whereas with 0.4 wt.% of agglomerated Y_2O_3 particles, the RD value is drastically decreased. In the case of the yttria-free alloy, the density value is only 0.7% lower than that of the 0.8 wt.% Y_2O_3 alloy. Therefore, these results are not only attributed to the morphology of the processed particles, but also to their fluidity. As it was already mentioned in the microscopy section, the alloy with 0.8 wt.% Y_2O_3 has fewer particle agglomerates, compared to its counterpart with 0.4 wt.% Y_2O_3, while the alloy without yttria is constituted by flaky particles. That is, the ODS alloy with the highest yttria content has a wider particle size distribution, which results in better packing of the particles when they are subjected to the sintering process. The low density reached by the 0.4 wt.% Y_2O_3 alloy series is attributed to the agglomerated state and clogging effect of the powder particles, which prevents adequate compaction during sintering.

Figure 9 reveals the type of microstructure developed by the powder containing 0 (a – d), 0.4 (b – e), and 0.8 wt.% Y_2O_3 (c – f), after milling for 60 min followed by sintering by SPS at 1100 °C. Micrographs d), e), and f) are magnifications of a), b), and c), respectively, to reveal the presence of black pores with semicircular morphology (indicated by the black arrows and letter P), as well as the presence of γ-Fe precipitates, which are identified by the letter G. In Fig. 9 (a, b, c), scattered narrow, and elongated white areas are distinguished, corresponding to W debris (red arrows). In micrographs b) and c), mainly, the presence of such traces of elemental W can be seen, elemental tungsten traces are part of the original powder precursor mix. It was observed that at short milling times of up to 15 min, W goes into a solid solution in the ferritic matrix, but at longer times it dissolves, up to a certain solubility limit. At longer milling times, using XRD, traces of W were detected in its elemental form (Figs. 3, 4 and 5), which is explained as W in stoichiometric excess, which remains mechanically dispersed in the matrix. From these micrographs, not only fine pores of less than 10 μm but also α- and γ-Fe precipitates are evenly distributed throughout the surface of the sintered samples.

The XRD patterns obtained for the three alloys whose powders were milled for 60 min and subsequently sintered by SPS are shown in Fig. 10. The sintered alloys show oxidation of chromium, since this element

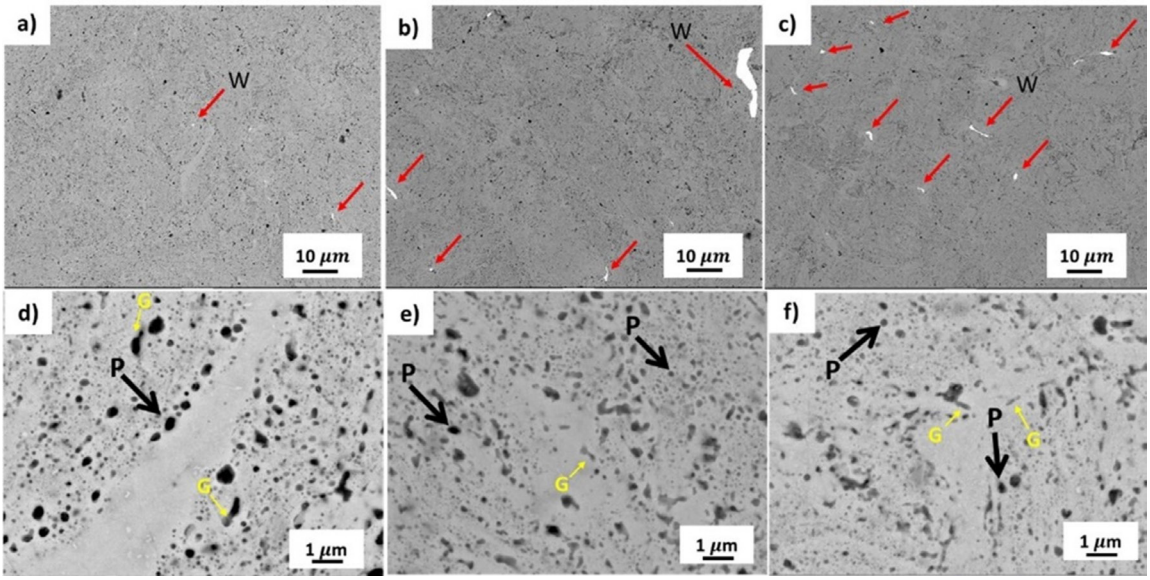

Figure 9. SEM micrographs of the powders processed by HEM for 60 min and subsequently sintered by SPS at 1100 °C, corresponding to the ODS ferritic alloy series containing: 0 (a – d), 0.4 (b – e), and 0.8 wt.% Y_2O_3 (c – f). Micrographs d), e), and f) are magnifications of micrographs a), b) and c), respectively. Black pores with semicircular geometries are indicated by the letter P. The presence of γ-Fe precipitates is indicated by the letter G and the presence of W is indicated by red arrows.

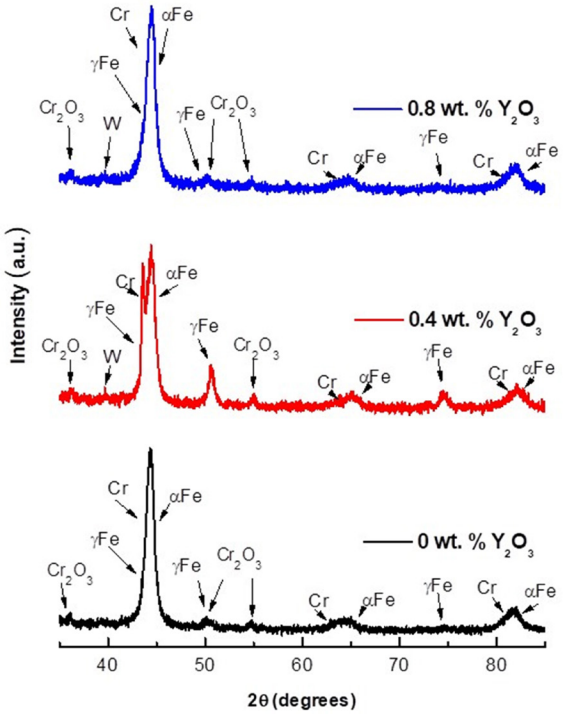

Figure 10. XRD patterns of the ODS ferritic powders milled for 60 min and sintered by SPS at 1100 °C, containing 0, 0.4, and 0.8 wt.% Y_2O_3.

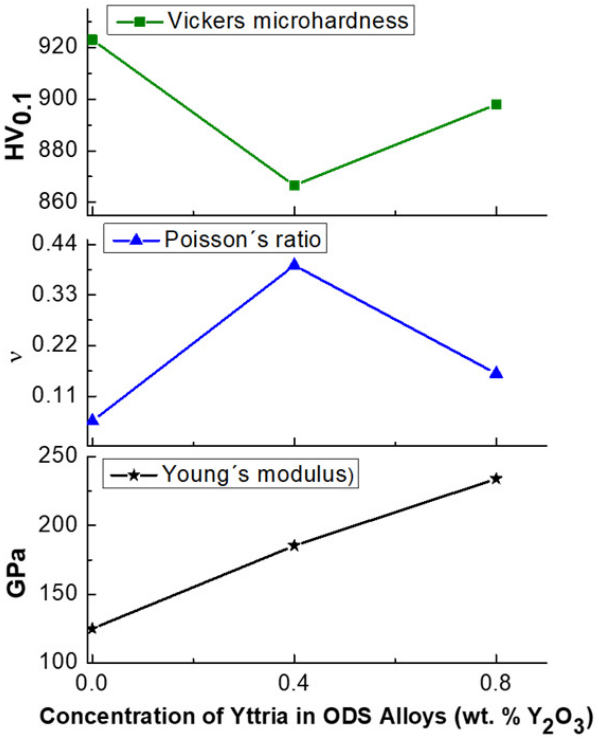

Figure 11. Mechanical properties of the ODS ferritic alloys with a dispersion of 0, 0.4 and 0.8 wt.% Y_2O_3, milled using HEM and sintered by SPS at 1100 °C. Young's modulus and Poisson"s ratio, dimensional shrinkage, and Vickers microhardness values are included.

has a higher affinity for oxygen when compared with Fe and other alloying elements (Yaskiv and Fedirko, 2014) so when these alloys are sintered at 1100 ˚C, a passive surface layer of Cr_2O_3 is formed. The analysis also revealed the presence of elemental traces of Cr and W, as well as of the α-Fe phase. Even though the austenite γ-Fe phase precipitated in the three alloys, the presence of this phase is only clear in the 0.4 wt.% Y_2O_3 alloyed. Under the processing and sintering conditions employed in this work, in these alloys, Fe grains have a fcc lattice structure (γ-Fe phase). Judging from the SEM micrographs shown in Fig. 10 and corresponding XRD patterns, it is evident that, upon sintering, the α- to γ-Fe phase transformation occurred through the formation of submicron-sized grains.

Some of the fundamental mechanical properties of the studied alloys are plotted in Fig. 11, as a function of their yttria content. These parameters are Young's modulus, Poisson's ratio, and Vickers microhardness. In general, except for the Poisson's ratio , the largest values of these properties are observed for the alloy containing 0.8 wt.% Y_2O_3.

For both Young's modulus and Poisson's ratio, the magnitude of the values obtained is related to the anisotropy of the microstructure as well as to the direction in which the measurement was made (Sánchez-Gutiérrez *et al.*, 2017). On the other hand, the low values of the Poisson ratio were due to the difference between the transverse deformation and the longitudinal deformation, the former being much lower than the latter.

The ODS alloy without yttria is the one that showed the lowest value of the elastic modulus, which is congruent with its highest hardness value. The ferritic alloy with 0.8 wt.% Y_2O_3 disclosed the least dimensional change as a function of temperature, whereas its 0.4 wt.% Y_2O_3 counterpart suffered both the greatest linear expansion and the major microstructural changes, which influences its elastic properties. The 0.4 wt.% Y_2O_3 alloy also disclosed the lowest hardness value and the smaller crystallite size (Fig. 6). As it can be seen in Fig. 11, the Young module rises as a function of the Y_2O_3 content in the alloy. Thus, the 0.4 wt.% Y_2O_3 alloy was more ductile than the 0.8 wt.% Y_2O_3 alloy.

These results agreed with Kumar *et al.* (2018), who conclude that contents of Y_2O_3 higher than 0.5 wt.% result in alloys with high hardness and high elastic modulus due to work hardening, generating microcracks that cause fractures, and, therefore, a lower ductility in the material.

When compared with other works (Dash *et al.*, 2018), where ODS ferritic alloys have been synthesized, and have also been densified using the SPS technique, it is found that the values obtained in the present study for the elastic modulus are 30% lower, particularly in the case of the 0.4 wt.% Y_2O_3 alloy. From the value of the Poisson's ratio reached by the latter alloy,

it is verified that this is the one undergoing the most deformation, particularly in some of its axes, when the compressive load is applied (Hook's law).

In Fig. 11 it is observed that the 0.4 wt.% Y_2O_3 alloy was the one showing the lowest Vickers microhardness value (865 HV), as well as the highest degree of porosity and the lowest relative density RD, among all the alloys studied. For comparison purposes, the experimental results of this work are included at the end of Table 1, along with those reported in the literature.

The addition of yttria particles into the ODS ferritic alloys leads to both a smaller and more homogeneous grain size. Moreover, the addition of Y_2O_3 particles hinders defects in the alloys, since it might occupy the room left for defects (interstitials and vacancies), occasionally avoiding the movement of dislocations in the crystalline structure (Kumar *et al.*, 2018).

The 0.4 wt.% Y_2O_3 alloy was found to be more ductile, which is consistent with what was mentioned by Kumar *et al.* (2018), who stated that a Y_2O_3 content greater than 0.5 wt.% reduces ductility. On the other hand, a greater presence of the austenite phase generates a volumetric increase when the phase change from ferrite to austenite occurs, modifying the microstructure and thus, affecting the resulting properties of the alloys. The high porosity remaining in the samples plays an important role in both ductility and hardness. The 0.4 wt.% Y_2O_3 alloy has a lower relative density (1.01%) than the 0.8 wt.% Y_2O_3 alloy, which is also a factor that decreases hardness.

The obtained alloys show a heterogeneous microstructure, thereby an anisotropic behavior would be expected, in such a way that, depending on the orientation or direction in which the specimens are placed for the measurement to be made, the value of the elastic modulus might change. In this respect, Sánchez-Gutiérrez *et al.* (2017) carried out a mathematical simulation study of an alloy with Y_2O_3 dispersion (Fe-18.6Cr-5.2Al-0.54Ti-0.04C-0.006N-0.5Y_2O_3). The calculations were made in the crystallographic directions x [100], y[110], and z[111], finding Young's modulus values of 131, 219 and 238 GPa, very close to those found (234 GPa) for the 0.8 wt.% Y_2O_3 alloy of this work.

A representative graph of the corrosion behavior recorded for the studied alloys, when tested in 1 M HNO_3, is presented in Fig. 12. Unlike both the 0.4 and 0.8 wt.% Y_2O_3 alloys, the anodic region of the potentiodynamic polarization curve (blue) obtained for the yttria-free alloy revealed the occurrence of two passivation events (P_1 and P_2), which are attributed to the formation of a Cr_2O_3 layer which momentarily protects the base alloy, until the P_3 trans passivation zone appears, indicating the breakdown of such protective layer. Meanwhile, the 0.4 and 0.8 wt.% Y_2O_3 alloys, whose current density is higher, showed similar behavior to each other (red and black curves), both showing a long-lasting trans passivation zone (TP), which protects the alloys during longer times, compared to the

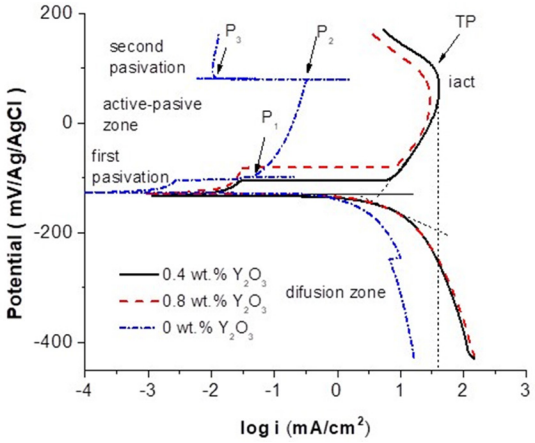

Figure 12. Potentiodynamic polarization curves for the ODS ferritic alloys containing 0, 0.4, and 0.8 wt.% Y_2O_3, sintered by SPS and corrosion tested in 1 M HNO_3.

yttria-free alloy. That is, even though the latter alloy exhibits a lower current density, in such a way that it also shows greater corrosion resistance, the fact that its protective layer breaks down before that formed at the surface of its yttria-containing counterparts makes it less effective

The fact of processing the precursor metallic powders, via high-energy ball milling (HEM) allows introducing microstructural defects into the ODS alloy matrix, leading the powder blend mixture into a highly mechano-activated state. The metastable state of the SPS-densified samples is somehow preserved after the rapid sintering, which in turn causes the ODS alloy to react eagerly. EDS analyses (Fig. 13) indicate that, after conducting the corrosion test, a Cr_2O_3 passive layer is formed on the surface of the alloy having no Y_2O_3, whereas in alloys with 0.4 and 0.8 wt.% Y_2O_3 oxides layers of Fe and Cr formed. The Cr layer preferentially expands the passivation zone, as revealed from the potentiodynamic polarization curve, thus associated with Y_2O_3. Thermodynamically, it is easier for some chemical states of iron to be reduced than oxidized, so comparatively in this case, chromium is energetically easier to oxidize, thus forming the protective chrome layer. The chemical affinity between Cr and Y was reported by Wang C. Zhen through the formation of $YCrO_3$ (Chang-Zhen *et al.*, 1985) . Although this compound is expected to form at high temperatures, through the reaction $Y_2O_3 + Cr_2O_3 \rightarrow 2YCrO_3$, the vigorous mechano-chemical action might eventually allow its formation. Owing to the limited proportion of yttrium oxide added to the ferritic alloy, the XRD pattern showing $YCrO_3$ is not obvious, but shows Cr_2O_3. Ningshen *et al.* (2014), claimed that Y_2O_3 promoted the formation of complex $Y_2Hf_2O_7$ oxide in 15% Cr ODS steel, and this oxide may have a role in suppressing intergranular corrosion attack. The addition of Y_2O_3 has also been reported to increase corrosion resistance in Al 6061 aluminum alloy (Ahmadi and Nouri, 2010). On the

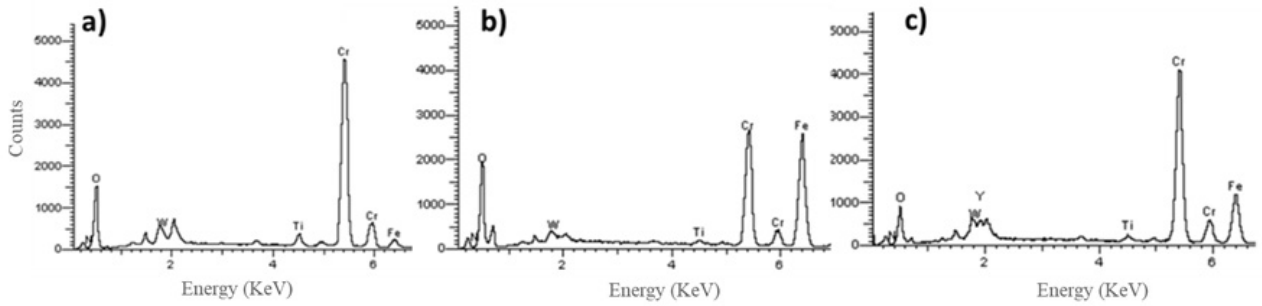

Figure 13. EDS spectra of the ferritic matrix after potentiodynamic analysis, corresponding to alloys a) 0 ODS-900, b) 0.4 ODS-900, and c) 0.8 ODS-900.

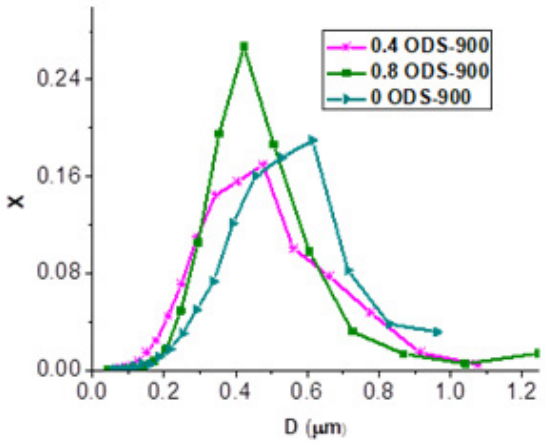

Figure 14. Variation of grain size vs accumulated volume, for the ODS ferritic alloy containing: 0.4, 0.8, and 0 wt.% Y_2O_3.

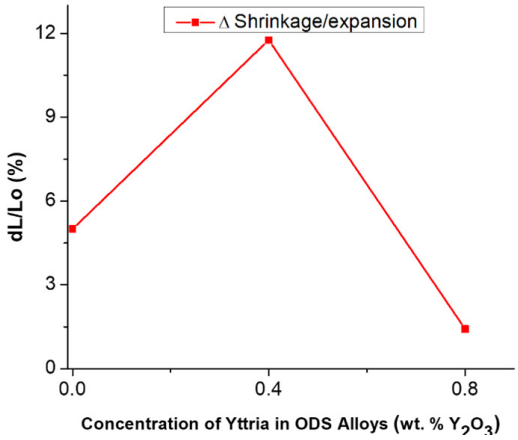

Figure 15. Dimensional shrinkage/expansion of the ODS ferritic alloys with a dispersion of 0, 0.4 and 0.8 wt.% Y_2O_3, milled using HEM and sintered by SPS a 1100 °C.

other hand, Y_2O_3 decreases the grain size (Fig. 14) and thus increases the grain boundary area. However, due to the nature of the more stable passive layer, this oxide increases the resistance to intergranular attack, which agrees with other results (Ningshen *et al.*, 2014).

Figure 12 shows three zones. The first one goes from the equilibrium potential to point P_1 and is related to the formation of a first passivation zone. The second one, corresponding to the so-called "active-passive zone", is related to the breakdown of the first passivation zone and extends from point P_1 to point P_2, and the third one, corresponding to the second passivation zone, extends from point P_2 to point P_3. Table 3 shows the values of current densities and potentials recorded at points P_1, P_2 and P_3.

For the Yttria-free alloy, the breakdown point is located at $10^{-1.30}$ mA·cm^{-2} and 96.9 mV vs E Ag/AgCl electrode. In comparison, the breakdown points of the Yttria-containing alloys are located at lower current density values ($10^{0.73}$ mA·cm^{-2} for the 0.4 wt.% Y_2O_3 alloy, and $10^{0.42}$ mA·cm^{-2} for the 0.8 wt.% Y_2O_3 alloy).

In the cathodic branch of the curve, the current limit density for oxygen is -$10^{1.19}$ mA·cm^{-2} for the alloy without yttria, and – $10^{2.057}$ mA·cm^{-2} and -$10^{2.11}$ mA·cm^{-2} for 0.4 wt.% and 0.8 wt.% Y_2O_3 alloys, respectively. Thus, the Yttria-containing alloys have more current density in the cathodic branch to balance the corrosion current density.

From Fig. 15 it is observed that the dimensional shrinkage/expansion, it is also possible to verify the effect of the longitudinal contraction suffered by the three alloys during the heat treatment, while the α → γ phase change takes place, as a function of the yttria

Table 3. Electrochemical key points of different zones on the potentiodynamic polarization curve of Fig. 12

Mixture code	i_1 (mA·cm^{-2})	E_1 vs Ag/AgCl (mV)	i_2 (mA·cm^{-2})	E_2 vs Ag/AgCl (mV)	i_3 (mA·cm^{-2})	E_3 vs Ag/AgCl (mV)
0 wt.% Y_2O_3	$10^{-1.30}$	-96.9	$10^{-0.58}$	78.24	$10^{-1.98}$	81.38
0.4 wt.% Y_2O_3	$10^{-1.53}$	-104.67	$10^{1.52}$	70.48	$10^{0.73}$	170.43
0.8 wt.% Y_2O_3	$10^{-1.53}$	-81.21	$10^{1.46}$	50.15	$10^{0.42}$	178.38

content. It is observed that the 0.8 wt.% Y_2O_3 alloy is the one exhibiting the least dimensional change, while the 0.4 wt.% Y_2O_3 alloy is the one undergoing the greatest expansion due to the influence of the phase transformation on its elastic properties. A higher content and therefore better dispersion of yttria particles in these alloys reduce the atomic movement in their crystal lattice, which leads to the generation of fewer micro-crystalline defects.

4. CONCLUSIONS

- Ferritic Fe-14Cr-1.5W-0.2Ti alloys were prepared with Y_2O_3 particles dispersed in their matrix, in concentrations of 0, 0.4, and 0.8 wt.%, by combining the HEM and SPS techniques.
- Both the morphology and size of the particles directly influenced the degree of densification reached by the alloys during sintering. The addition of 0.8 wt.% Y_2O_3 to the ferritic alloy led to an increase in its relative density RD (up to 94.5%), whereas it sharply decreased with 0.4 wt.% Y_2O_3. In the case of the yttria-free alloy, the density value was only 0.7% lower than that obtained for the 0.8 wt.% Y_2O_3 alloy. These results were attributed to both the morphology of the milled particles and the presence of particle agglomerates.
- The lattice parameter value of the α-Fe phase was found to depend on the yttria content of the alloy as well as on the sintering process. In the case of the 0.4 wt.% Y_2O_3 alloy, a reduction of the lattice parameter was associated with a greater reinforcement of the α-Fe matrix by the dispersed oxides.
- According to the potentiodynamic polarization studies carried out, it was found that the protective layer of Cr_2O_3 formed on the surface of the three alloys studied was less effective for the yttria-free alloy since in this case, the rupture of such protective layer occurred earlier than for the case of the yttria-containing alloys.
- The 0.8 wt.% Y_2O_3 alloy was the one with the least dimensional change as a function of temperature, while the 0.4 wt.% Y_2O_3 alloy was the one undergoing the greatest expansion and microstructural changes, which influences its elastic properties.
- The largest values of Poisson ratio, and dimensional shrinkage/expansion were obtained for the 0.4 wt.% Y_2O_3 alloy. The ODS alloy without yttria was the one showing the lowest elastic modulus and the highest hardness degree. These results were attributed to the homogeneous dispersion of the oxide and the presence of the γ-Fe phase in the alloys. The 0.4 wt.% Y_2O_3 alloy was more ductile than the other two alloys. A similar trend was observed regarding the elastic and Poisson's moduli for all the materials studied. It is suggested that the alloys with 0.8 wt.% Y_2O_3 and fine microstructure could constitute potential alternatives as structural materials for Gen IV-type reactors.

ACKNOWLEDGMENTS

Authors acknowledge CINVESTAV Saltillo, Instituto Politécnico Nacional (IPN), CIITEC-IPN, Escuela Militar de Ingenieros EMI-Popotla in Mexico City, Instituto Nacional de Investigaciones Nucleares (ININ), and CONACYT Mexico, Mexican institutions which made possible the conduction of this research work. ARSR acknowledges CONACYT for a doctor scholarship. SDT and JCMG acknowledge SIP-COFAA-IPN through projects 20230119 and 20230411. The authors also acknowledge A. Patiño Pineda of CIITEC-IPN for his assistance in preparing the SPS specimens,, O. Gutiérrez Obeso for the HEM facilities, R. Ambriz Rojas for Young's modulus tests, J.C. Zenteno Juárez of ININ for his assistance in preparing specimens for corrosion testing, and F. Marquez, and L.M. Madero Negrete of CINVESTAV Saltillo for their assistance in metallographic preparation.

REFERENCES

Abenojar, J., Velasco, F., Martínez, M.A. (2006). Manufacturing of Porous Boron Steels Potentially Useful as Nuclear Materials. *J. Nucl. Sci. Technol.* 43 (8), 866–873. https://www.tandfonline.com/doi/abs/10.1080/18811248.2006.9711171.

Ahmadi, H., Nouri, M. (2010). Beneficial effects of yttrium on mechanical failure and chemical stability of the passive film in 6061 aluminum alloy. *J. Mater. Sci.* 45 (13), 3426–3432. https://doi.org/10.1007/s10853-010-4368-9.

Auger, M.A., De Castro, V., Leguey, T., Muñoz, A., Pareja, R. (2013). Microstructure and mechanical behavior of ODS and non-ODS Fe–14Cr model alloys produced by spark plasma sintering. *J. Nucl. Mater.* 436 (1-3), 68–75. https://doi.org/10.1016/j.jnucmat.2013.01.331.

Buchanan, R.A., Stansbury, E.E. (2012). 4 - *Electrochemical Corrosion. In Handbook of Environmental Degradation of Materials*. Second Edition, William Andrew Publishing, pp. 87–125. https://doi.org/10.1016/B978-1-4377-3455-3.00004-3.

Cayron, C., Rath, E., Chu, I., Launois, S. (2004). Microstructural evolution of Y_2O_3 and $MgAl_2O_4$ ODS EUROFER steels during their elaboration by mechanical milling and hot isostatic pressing. *J. Nucl. Mater.* 335 (1), 83–102. https://doi.org/10.1016/j.jnucmat.2004.06.010.

Chang-Zhen, W., Shu-Qhing, Y., Xin, Z. (1985). A Study On Thermodynamic Properties Of Y_2O_3·Cr_2O_3 Compound. *Acta Phys. Sin.* 34 (8), 1017-1026. https://doi.org/10.7498/aps.34.1017.

Dash, M.K., Mythili, R., Ravi, R., Sakthivel, T., Dasgupta, A., Soroja, S., Bakshi, S.R. (2018). Microstructure and mechanical properties of oxide dispersion strengthened 18Cr-ferritic steel consolidated by spark plasma sintering. *Mater. Sci. Eng. A* 736, 137–147. https://doi.org/10.1016/j.msea.2018.08.093.

Dharmalingam, G., Mariappan, R., Arun Prasad, M. (2018). Microstructure and Mechanical Properties of Hot Pressed 16.5CR Ferritic ODS Steel Developed Through Mechanical Alloying. *IJMPERD* 8 (2), 699–708. https://doi.org/10.24247/ijmperdapr201882.

Fu, J., Brouwer, J.C., Richardson, I.M., Hermans, M.J.M. (2019). Effect of mechanical alloying and spark plasma sintering on the microstructure and mechanical properties of ODS Eurofer. *Mater. Des.* 177, 107849. https://doi.org/10.1016/j.matdes.2019.107849.

Gao, R., Zhang, T., Wang, X.P., Fang, Q.F., Liu, C.S. (2014). Effect of zirconium addition on the microstructure and mechanical properties of ODS ferritic steels containing aluminum. *J. Nucl. Mater.* 444 (1-3), 462–468. https://doi.org/10.1016/j.jnucmat.2013.10.038.

Grimes, R.W., Konings, R.J.M., Edwards, L. (2008). Greater tolerance for nuclear materials. *Nat. Mater.* 7 (9), 683–685. https://doi.org/10.1038/nmat2266.

Hilger, I., Bergner, F., Weißgärber, T. (2015). *Bimodal Grain Size Distribution of Nanostructured Ferritic ODS Fe-Cr Alloys. In Sintering 2014.* Wiley Subscription Services, Inc., 98 (11), pp. 3576-3581. https://doi.org/10.1111/jace.13833.

Hilger, I., Boulnat, X., Hoffmann, J., Testani, C., Bergner, F., De Carlan, Y., Ferraro, F., Ulbricht, A. (2016). Fabrication and characterization of oxide dispersion strengthened (ODS) 14Cr steels consolidated by means of hot isostatic pressing, hot extrusion and spark plasma sintering. *J. Nucl. Mater.* 472, 206–214. https://doi.org/10.1016/j.jnucmat.2015.09.036.

Karak, S.K., Dutta Majumdar, J., Lojkowski, W., Michalski, A., Ciupinski, L., Kurzydlowski, K.J., Manna, I. (2012). Microstructure and mechanical properties of nano-Y2O3 dispersed ferritic steel synthesized by mechanical alloying and consolidated by pulse plasma sintering. *Philos. Mag.* 92 (5), 516–534. https://doi.org/10.1080/14786435.2011.619508.

Kumar, D., Prakash, U., Dabhade, V.V., Laha, K., Sakthivel, T. (2017). High yttria ferritic ODS steels through powder forging. *J. Nucl. Mater.* 488, 75–82. https://doi.org/10.1016/j.jnucmat.2016.12.043.

Kumar, D., Prakash, U., Dabhade, V.V., Laha, K., Sakthivel, T. (2018). Influence of Yttria on Oxide Dispersion Strengthened (ODS) Ferritic Steel. *Mater. Today: Proc.* 5 (2, Part 1), 3909–3913. https://doi.org/10.1016/j.matpr.2017.11.646.

Mihalache, V., Mercioniu, I., Velea, A., Palade, P. (2019). Effect of the process control agent in the ball-milled powders and SPS-consolidation temperature on the grain refinement, density and Vickers hardness of Fe14Cr ODS ferritic alloys. *Powder Technol.* 347, 103–113. https://doi.org/10.1016/j.powtec.2019.02.006.

Ningshen, S., Sakairi, M., Suzuki, K., Ukai, S. (2014). The corrosion resistance and passive film compositions of 12% Cr and 15% Cr oxide dispersion strengthened steels in nitric acid media. *Corros. Sci.* 78, 322–334. https://doi.org/10.1016/j.corsci.2013.10.015.

Noh, S., Choi, B.K., Kang, S.H., Kim, T. (2014). Influence of mechanical alloying atmospheres on the microstructures and mechanical properties of 15Cr ODS steels. *Nucl. Eng. Technol.* 46 (6), 857–862. https://doi.org/10.5516/NET.07.2013.096.

Oksiuta, Z., Olier, P., De Carlan, Y., Baluc, N. (2009). Development and characterisation of a new ODS ferritic steel for fusion reactor application. *J. Nucl. Mater.* 393 (1), 114–119. https://doi.org/10.1016/j.jnucmat.2009.05.013.

Park, J.J., Hong, S.M., Park, E.K., Lee, M.K., Rhee, C.K. (2012). Synthesis of Fe based ODS alloys by a very high speed planetary milling process. *J. Nucl. Mater.* 428 (1-3), 35–39. https://doi.org/10.1016/j.jnucmat.2011.12.027.

Perera, F. (2017). Pollution from fossil-Fuel combustion is the leading environmental threat to global pediatric health and equity: Solutions Exist. *Int. J. Environ. Res. Public Health* 15 (1), p. 16. https://doi.org/10.3390/ijerph15010016.

Rajan, K., Sarma, V.S., Kutty, T.R.G., Murty, B.S. (2012). Hot hardness behaviour of ultrafine grained ferritic oxide dispersion strengthened alloys prepared by mechanical alloying and spark plasma sintering. *Mater. Sci. Eng. A* 558, 492–496. https://doi.org/10.1016/j.msea.2012.08.033.

Rajan, K., Shanmugasundaram, T., Subramanya Sarma, V. Murty, B.S. (2013). Effect of Y_2O_3 on Spark Plasma Sintering Kinetics of Nanocrystalline 9Cr-1Mo Ferritic Oxide Dispersion-Strengthened Steels. *Metall. Mater. Trans. A* 44 (9), 4037–4041. https://doi.org/10.1007/s11661-013-1845-1.

Ramanujam, A. (2001). *Purex and Thorex Processes (Aqueous Reprocessing). In Encyclopedia of Materials: Science and Technology*. Second Edition, Buschow, K.H.J., Cahn, R.W., Flemings, M.C., Ilschner, B., Kramer, E.J., Mahajan, S., Veyssière, T. (Ed.), Elsevier, pp. 7918–7924. https://doi.org/10.1016/B0-08-043152-6/01426-1.

Sánchez-Gutiérrez, J., Chao, J., Vivas, J., Galvez, F., Capdevila, C. (2017). Influence of texture on impact toughness of ferritic Fe-20Cr-5Al oxide dispersion strengthened steel. *Materials* 10 (7), 745. https://doi.org/10.3390/ma10070745.

Sun, Q.X., Zhang, T., Wang, X.P., Fang, Q.F., Hao, T., Liu, C.S. (2012). Microstructure and mechanical properties of oxide dispersion strengthened ferritic steel prepared by a novel route. *J. Nucl. Mater.* 424 (1-3), 279–284. https://doi.org/10.1016/j.jnucmat.2011.12.020.

Torralba, J.M., Fuentes-Pacheco, L., García-Rodríguez, N., Campos, M. (2013). Development of high performance powder metallurgy steels by high-energy milling. *Adv. Powder Technol.* 24 (5), 813–817. https://doi.org/10.1016/j.apt.2012.11.015.

Verhiest, K., Al Mazouzi, A., De Wispelaere, N., Petrov, R., Claessens, S. (2009). Development of oxides dispersion strengthened steels for high temperature nuclear reactor applications. *J. Nucl. Mater.* 385 (2), 308–311. https://doi.org/10.1016/j.jnucmat.2008.12.006.

Yamamoto, M., Ukai, S., Hayashi, S., Kaito, T., Ohtsuka, S. (2010). Formation of residual ferrite in 9Cr-ODS ferritic steels. *Mater. Sci. Eng. A* 527 (16–17), 4418–4423. https://doi.org/10.1016/j.msea.2010.03.079.

Yaskiv, O.I., Fedirko, V.M (2014). Oxidation/Corrosion Behaviour of ODS Ferritic/Martensitic Steels in Pb Melt at Elevated Temperature. *Int. J. Nucl. Energy* ID 657689, 1–8. https://doi.org/10.1155/2014/657689.

Zhang, H., Huang, Y., Ning, H., Williams, C.A., London, A.J., Dawson, K., Hong, Z., Gorley, M.J., Grovenor, R.M., Tatlock, G.J., Roberts, S.G., Reece, M.J., Yan, H., Grant, P.S. (2015). Processing and microstructure characterisation of oxide dispersion strengthened Fe–14Cr–0.4Ti–0.25Y_2O_3 ferritic steels fabricated by spark plasma sintering. *J. Nucl. Mater.* 464, 61–68. https://doi.org/10.1016/j.jnucmat.2015.04.029.

Zhou, X., Liu, Y., Qiao, Z., Guo, Q., Liu, Ch., Yu, L., Li, H. (2017). Effects of cooling rates on δ-ferrite/γ-austenite formation and martensitic transformation in modified ferritic heat resistant steel. *Fusion Eng. Des.* 125, 354–360. https://doi.org/10.1016/j.fusengdes.2017.05.095.

Zinkle, S.J., Busby, J.T. (2009). Structural materials for fission & fusion energy. *Materials Today* 12 (11), 12–19. https://doi.org/10.1016/S1369-7021(09)70294-9.

Zinkle, S.J., Boutard, J.L., Hoelzer, D.T., Kimura, A., Lindau, R., Odette, G.R., Rieth, M., Tan, L., Tanigawa, H. (2017). Development of next generation tempered and ODS reduced activation ferritic/martensitic steels for fusion energy applications. *Nuclear Fusion* 57 (9), 092005. https://doi.org/10.1088/1741-4326/57/9/092005.